



Supplementary Materials for
**Direct electrosynthesis of pure aqueous H₂O₂ solutions up to 20%
by weight using a solid electrolyte**

Chuan Xia*, Yang Xia*, Peng Zhu, Lei Fan, Haotian Wang†

*These authors contributed equally to this work.

†Corresponding author. Email: htwang@rice.edu

Published 11 October 2019, *Science* **366**, 226 (2019)

DOI: 10.1126/science.aay1844

This PDF file includes:

Materials and Methods

Figs. S1 to S15

Supplementary Text

Table S1

References

Materials and Methods

Material synthesis

Preparation of functionalized carbon black. In a typical synthesis, 600 mg of commercial carbon black (XC-72, FuelCellStore) were added into 600 mL of 12.0 M nitric acid. Then, the above solution was refluxed at 85 °C for 1, 3 and 12 h to obtain oxidized carbon black with surface oxygen content of 7.33%, 10.19% and 11.62%, respectively. After natural cooling, the slurry was taken out, centrifuged and washed with water and ethanol until the pH was neutral. Finally, the sample was dried at 70 °C in a vacuum oven. The as-received commercial carbon black shows a 2.33% surface oxygen content. Furthermore, 500 mg of commercial carbon black was annealed in a tube furnace at a temperature of 500 °C for 2 h under a mixed hydrogen (5%)/argon atmosphere to obtain the surface oxygen-free carbon black.

Direct electrosynthesis of pure H₂O₂

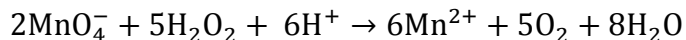
All the electrochemical measurements were run at 25 °C. A BioLogic VMP3 workstation was employed to record the electrochemical response. The typical three-electrode measurements were performed using a conventional flow cell (54). For aqueous electrolyte test, around 0.46 mg cm⁻² CB-10% catalyst was loaded on Sigracet 35 BC GDL electrode (Fuel Cell Store) as the cathode. Around 0.46 mg cm⁻² IrO₂ catalyst (Fuel Cell Store) was loaded on Sigracet 35 BC GDL electrode as the anode for water oxidation. The two electrodes were therefore placed on opposite sides of two 0.5 cm thick PTFE sheets with 0.5 cm wide by 2.0 cm long channels such that the catalyst layer interfaced with the flowing liquid electrolyte. A Nafion 115 film (Fuel Cell Store) was sandwiched by the two PTFE sheets to separate the chambers. The geometric surface area of catalyst is 1 cm². On the cathode side a titanium gas flow chamber supplied 20 sccm humidified O₂. The anode was circulated with 1 M Na₂SO₄ and 1 M KOH under a flow-rate of 2 mL min⁻¹ for O₂ reduction in 1 M Na₂SO₄ and 1 M KOH, respectively. A saturated calomel electrode (SCE, CH Instruments) was used as the reference electrode. For three-electrode measurement using solid electrolyte, around 0.46 mg cm⁻² CB-10% catalyst was loaded on Sigracet 35 BC GDL electrode (Fuel Cell Store) as the cathode. Around 0.46 mg cm⁻² 20% Pt-C catalyst (Fuel Cell Store) was loaded on Sigracet 35 BC GDL electrode as the anode for hydrogen oxidation. The cathode chamber in the flow cell was filled with solid polymer proton conductor, in a close contact with SCE reference electrode. AEM was used to separate the solid electrolyte and cathode electrode. CEM was employed to separate the solid electrolyte and anode electrode.

All potentials measured against SCE was converted to the reversible hydrogen electrode (RHE) scale in this work using $E_{\text{RHE}} = E_{\text{SCE}} + 0.244 \text{ V} + 0.0591 \times \text{pH}$, where pH values of electrolytes were determined by Orion 320 PerpHecT LogR Meter (Thermo Scientific). 1 M Na₂SO₄ (pH = 7) and 1 M KOH (pH = 14) were used as aqueous electrolyte. The flow-rate for the aqueous electrolyte is 27 mL h⁻¹ controlled by a syringe pump. The styrene-divinylbenzene sulfonated copolymer (36, 55) was employed as solid polymer electrolyte. In the solid electrolyte case, an anion exchange membrane (Dioxide Materials and Membranes International Inc.) was added between the solid electrolyte and the CB-10% catalyst to avoid flooding. The DI flow-rate through the porous solid electrolyte, which was used to bring out the generated H₂O₂, was also 27 mL h⁻¹ controlled by a syringe

pump. Solution resistance (R_s) was determined by potentiostatic electrochemical impedance spectroscopy (PEIS) at frequencies ranging from 0.1 Hz to 200 kHz. All the measured potentials using three-electrode setup were manually 100% compensated.

For the two-electrode cell for direct electrosynthesis of H_2O_2 , an anion exchange membrane (Dioxide Materials and Membranes International Inc.) and a Nafion film (Fuel Cell Store) were used for anion and cation exchange, respectively. Around 0.46 mg cm^{-2} CB-10% and Pt-C loaded on Sigracet 35 BC GDL electrode (4 cm^2 electrode area) were used as cathode and anode, respectively. The cathode side was supplied with 50 sccm of humidified O_2 gas (or air). The anode side was supplied with 50 sccm of humidified H_2 gas, or circulated with 0.5 M H_2SO_4 aqueous solution at 2 mL min^{-1} . Note that IrO_2 was used as anode catalyst instead of Pt-C when the anode was circulated with sulfuric acid solution for water oxidation. The styrene-divinylbenzene sulfonated copolymer (36, 55), inorganic $Cs_xH_{3-x}PW_{12}O_{40}$ proton conductor (56) or Dowex 1×8 (Sigma) anion conductor were used as solid ion conductors. The cell configurations were schematically illustrated in Fig. 1B and fig. S1. The $O_2//SE//H_2$ cell was firstly stabilized for 30 minutes before liquid product collection. To extend the stability of the $O_2//SE//H_2$ cell, we employed a reinforced AEM (AMI-7001, Membranes International Inc.), which is more mechanically robust compared to non-reinforced alternatives, for long-term operation test. All the measured potentials using two-electrode setup were manually 70% compensated unless stated otherwise.

The generated H_2O_2 concentration was evaluated using standard potassium permanganate (0.1 N $KMnO_4$ solution, Sigma-Aldrich) titration process, according to following equation:



In this work, sulfuric acid (2.0 N H_2SO_4 , VWR) was used as the H^+ source. After 10 min electrolysis under certain conditions, 10.0 mL liquid product was collected for $KMnO_4$ titration. The highest volume resolution by pre-calibrated pipet is $5 \mu\text{L}$, which gives a less than 2% error during titration process. The Faradaic efficiency (FE) for H_2O_2 production is calculated using following equation:

$$FE = \frac{\text{generated } H_2O_2 \text{ (mol L}^{-1}\text{)} \times 2 \times 96485 \text{ (C mol}^{-1}\text{)} \times \text{flow rate (mL s}^{-1}\text{)}}{j_{total}(\text{mA})} * 100$$

The rotation ring disk electrode (RRDE) measurements were run at 25°C in a typical three-electrode cell in 0.1 M Na_2SO_4 electrolyte. A carbon rod (99.99 %, Beantown Chemical) and a saturated calomel electrode (SCE, CH Instruments) were used as the counter and reference electrode, respectively. A RRDE assembly (AFE6R1PTPK, Pine Instruments) consisting of a glassy carbon rotation disk electrode ($\Phi = 5.0 \text{ mm}$) and a Pt ring ($\Phi = 15.0 \text{ mm}$) was used, with a theoretical collection efficiency of 25%. Experimentally, the apparent collection efficiency (N) was calibrated to be 24.1% in the ferrocyanide/ferricyanide half reaction system at a rotation rate between 400 and 2025 rpm. To prepare carbon black cast working electrode, typically, 3.3 mg of as-prepared CB-10% catalyst was mixed with 1 mL of ethanol and $10 \mu\text{L}$ of Nafion 117 solution (5 %, Sigma-

Aldrich), and sonicated for 20 min to get a homogeneous catalyst ink. 6 μL of the ink was pipetted onto glassy carbon disk (0.196 cm^2 area, 0.1 mg cm^{-2} mass loading), and was got vacuum dried prior to usage. As the catalyst can be dispersed very well in ethanol solutions, uniform catalyst coating can be made on the disc electrode without obvious pin holes or uncovered edge. All potentials measured against SCE was converted to the reversible hydrogen electrode (RHE) scale in this work using $E(\text{vs. RHE}) = E(\text{vs. SCE}) + 0.244\text{ V} + 0.0591 \times \text{pH}$, where pH values of electrolytes were determined by Orion 320 PerpHecT LogR Meter (Thermo Scientific). H_2O_2 selectivity was calculated using the following equation: $\text{H}_2\text{O}_2(\%) = 200 \times \frac{I_{\text{ring}}/N}{I_{\text{disk}} + I_{\text{ring}}/N}$, where I_{ring} is the ring current, I_{Disk} is the disk current and N is the collection efficiency.

Characterization

X-ray photoelectron spectroscopy was obtained with a PHI Quantera spectrometer, using a monochromatic Al $K\alpha$ radiation (1486.6 eV) and a low energy flood gun as neutralizer. All XPS spectra were calibrated by shifting the detected carbon C 1s peak to 284.6 eV. BET surface area analysis was performed using Quantachrome Autosorb-iQ-MP/Kr BET Surface Analyzer. SEM was performed on a FEI Quanta 400 field emission scanning electron microscope. Inductively coupled plasma atomic emission spectroscopy (ICP-OES) results were collected using Optima 8300 spectrometer. The rainwater was collected at Rice campus during Jan. 22, 2019 to Jan. 31, 2019. The total organic carbon (TOC) tests were done by a third-party company (A & B Lab) at Houston, Texas.

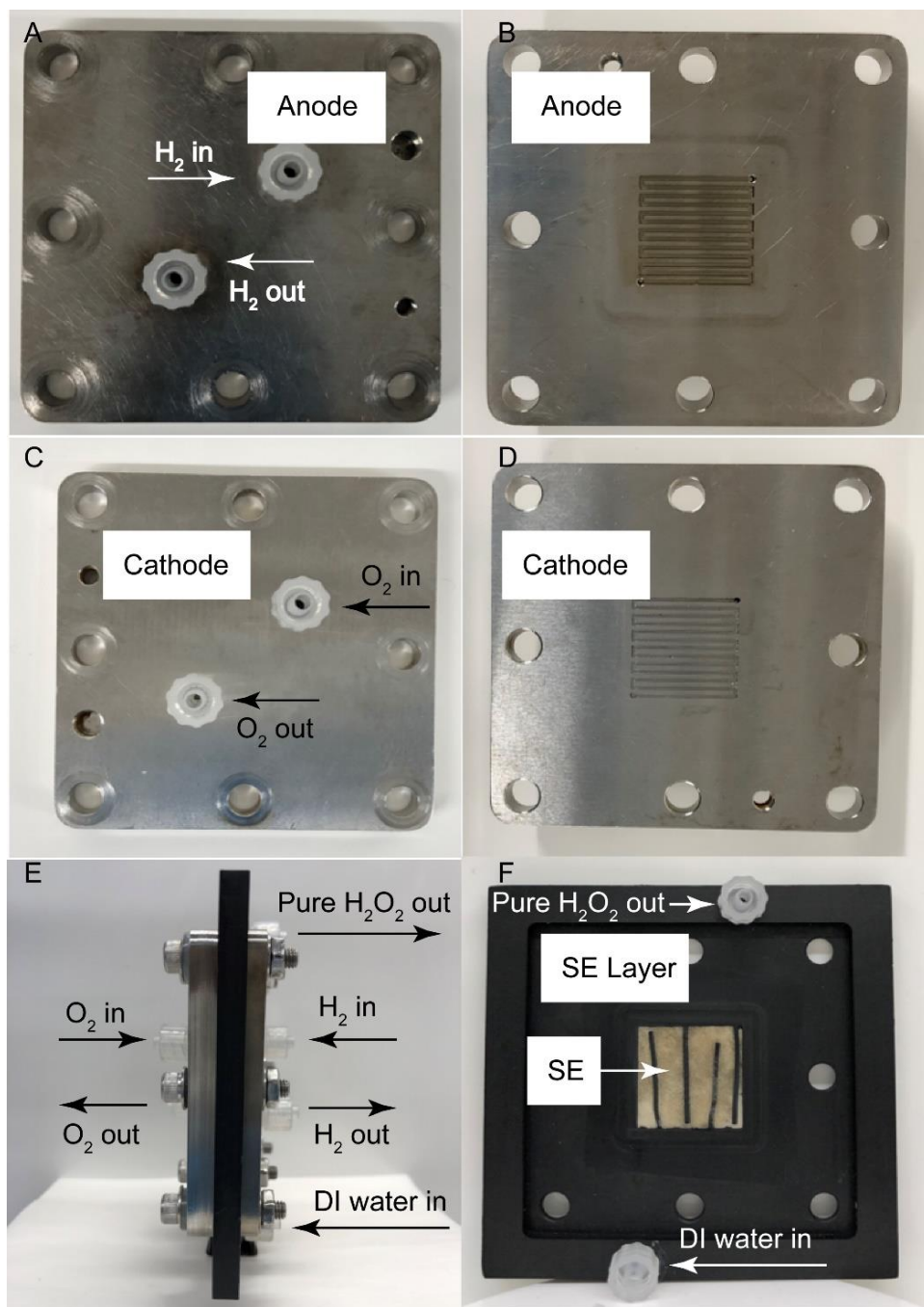


Fig. S1.

Digital photos of $O_2//SE//H_2$ cell. The front and back view of the (A, B) anode and (C, D) cathode electrode. (E) Side view of the assembled cell. (F) The front view of the solid electrolyte layer, where the sulfonated styrene-divinylbenzene copolymer microspheres were densely filled into the solid electrolyte thin layer. Note that the thickness of the solid electrolyte layer is 1.5 mm.

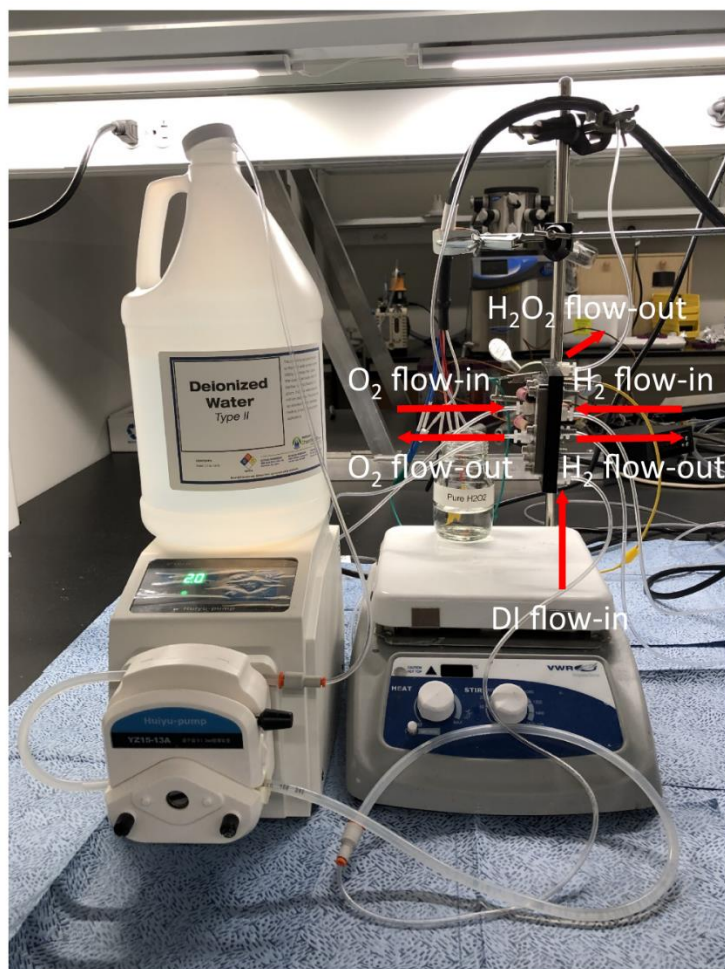


Fig. S2.

An overview of the system approach used in the experiments.

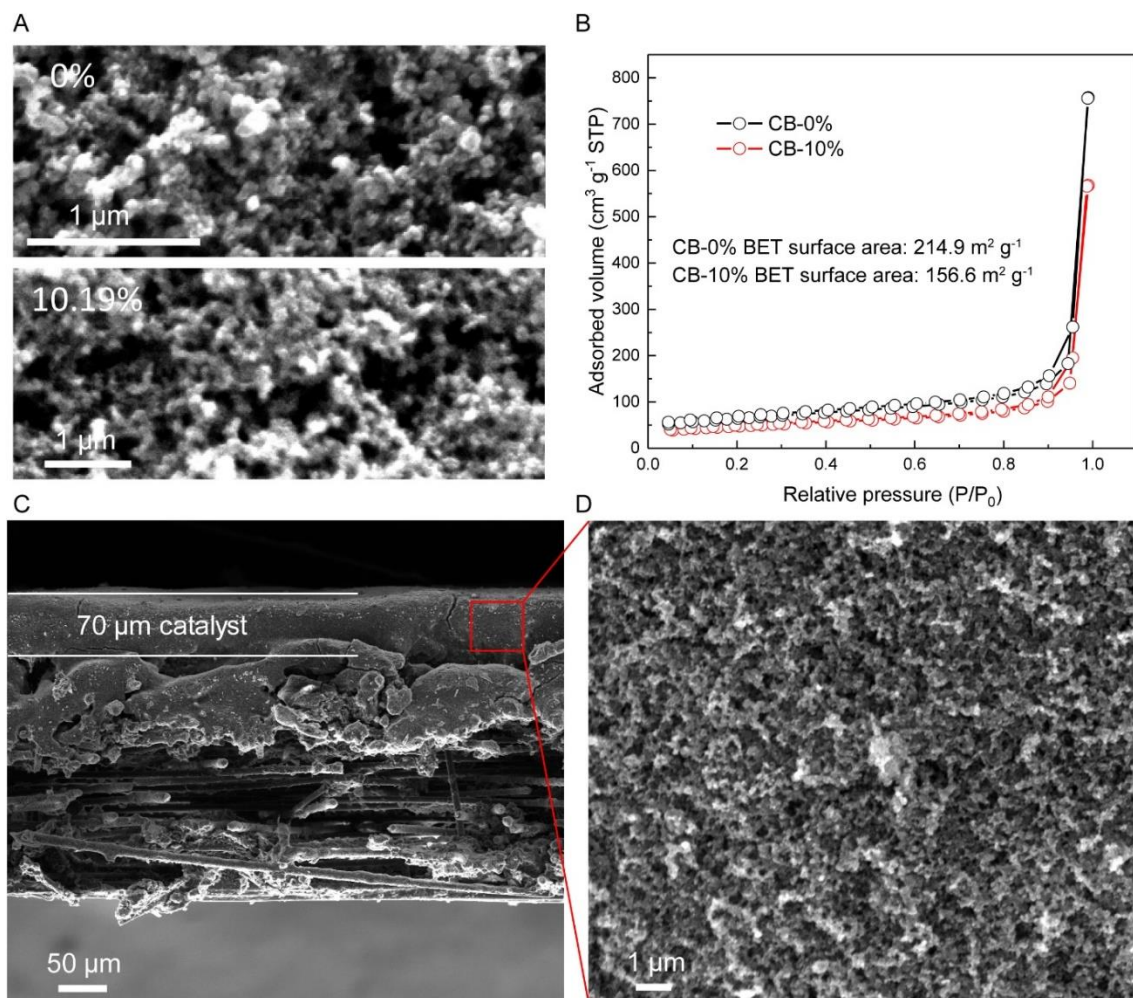


Fig. S3.

Characterization of carbon black catalyst. (A) SEM image and (B) BET surface area analysis of carbon-black catalyst with different surface oxygen content. The results show that there is no significant morphology evolution for carbon black catalyst after surface functionalization. (C) Representative SEM image of spray-coated CB-10% electrode, showing a $\sim 70 \mu\text{m}$ thick catalyst layer. (D) Enlarged SEM of the CB-10% catalyst electrode. It demonstrates that the catalyst layer on the GDL is highly porous, which is beneficial for fast O_2 diffusion and thus leads to improved catalytic current density.

Generally, in many cases after the oxidation or activation processes, carbon materials present higher surface areas. This can be easily observed particularly in cases where the starting carbon material is less defective such as graphite or solid carbon particles. However in our case, our starting carbon black is porous. While the oxidation process will introduce abundant defects, it could cause the collapse of the pore structure in the porous carbon black which will decrease the BET surface area. The BET data showed that the pore volume of the pristine carbon (CB-0%) is $71 \text{ cm}^3 \text{ g}^{-1}$ whereas that of the CB-10% sample is $52.2 \text{ cm}^3 \text{ g}^{-1}$. Thus, it is reasonable that the BET surface area of CB-0% ($214.9 \text{ m}^2 \text{ g}^{-1}$) is

higher than that of functionalized CB-10% ($156.6 \text{ m}^2 \text{ g}^{-1}$) as shown in fig. S3. This phenomenon has also been reported before ["Oxidation of different microporous carbons by chemical and electrochemical methods." *Frontiers in Materials* 6 (2019): 130]. We found that all the functionalized samples showed similar BET surface area (in the range of $150\text{-}170 \text{ m}^2 \text{ g}^{-1}$). We believe that the surface area does not play a critical role for the H_2O_2 activity enhancement, since the CB-10% with slightly lower BET surface area ($156.6 \text{ m}^2 \text{ g}^{-1}$) delivered better ORR activity compared to CB-2.11% ($167.3 \text{ m}^2 \text{ g}^{-1}$). We believe that the enhanced ORR activity originated from the increased active site density.

The ability of oxidized carbon for selective 2e^- -ORR has been reported before, including previous studies in possible active sites as also mentioned on Page 6 in our manuscript. Based on this previous knowledge, and considering the practical application of our design, we chose to oxidize commercial carbon black as the 2e^- -ORR catalyst mainly due to the following reasons. First, compared to other carbon materials such as graphene or CNTs used in previous reports [ref. 15-17], carbon black is thousands of times cheaper, and can be produced in a large scale. Second, carbon black is a form of paracrystalline carbon with defects or edges exposed, making the surface functionalization easier than graphene or CNT. For example, under the same oxidation reaction conditions, after 3-h oxidation our carbon black presents a 10% oxygen coverage, while CNT has only about 3% [ref. 16]. In addition, compared to other multi-step catalyst synthesis methods [ref. 15, 17, 18], this one-step functionalization process under mild conditions (85°C , 3h) also makes our catalyst preparation economical. Third, carbon black has a high surface area which can expose high density of active sites for large ORR current densities. Lastly, its nanoparticulate morphology facilitates O_2 diffusion from the GDL (layer-by-layer stacking of graphene nanosheets, by contrast, can hinder gas transport).

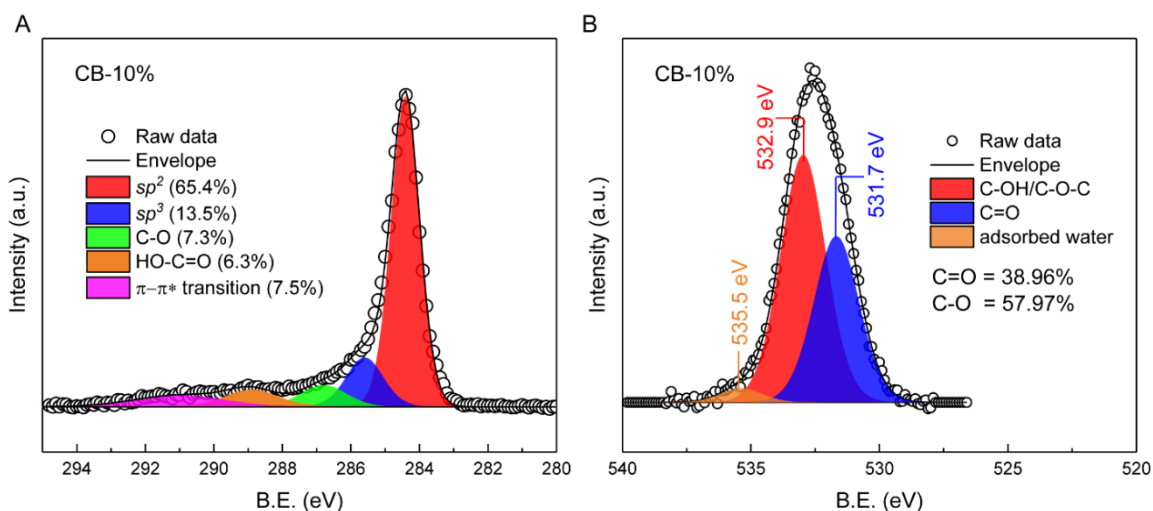


Fig. S4.

XPS characterization of CB-10% catalyst. High-resolution (A) C 1s (B) O 1s XPS spectra. The carbon 1s spectrum of the CB-10% catalyst can be deconvoluted into five contributions that are sp^2 carbon at 284.6 eV, sp^3 carbon at 285.5 eV, C-O at 286.8 eV, -COOH at 288.9 eV and the characteristic shakeup line of carbon in aromatic compounds at 291.2 eV ($\pi-\pi^*$ transition) (57, 58). The O 1s peaks could be deconvoluted into three peaks. According to the literature (59, 60), the components centered at 531.7 and 532.9 eV were attributed to the C-OH/C-O-C and C=O surface functional groups, respectively. The last component with B.E. around 535.5 eV was characteristic of adsorbed water. These results indicate that the acid treatment induced surface oxygen functionalization of carbon black.

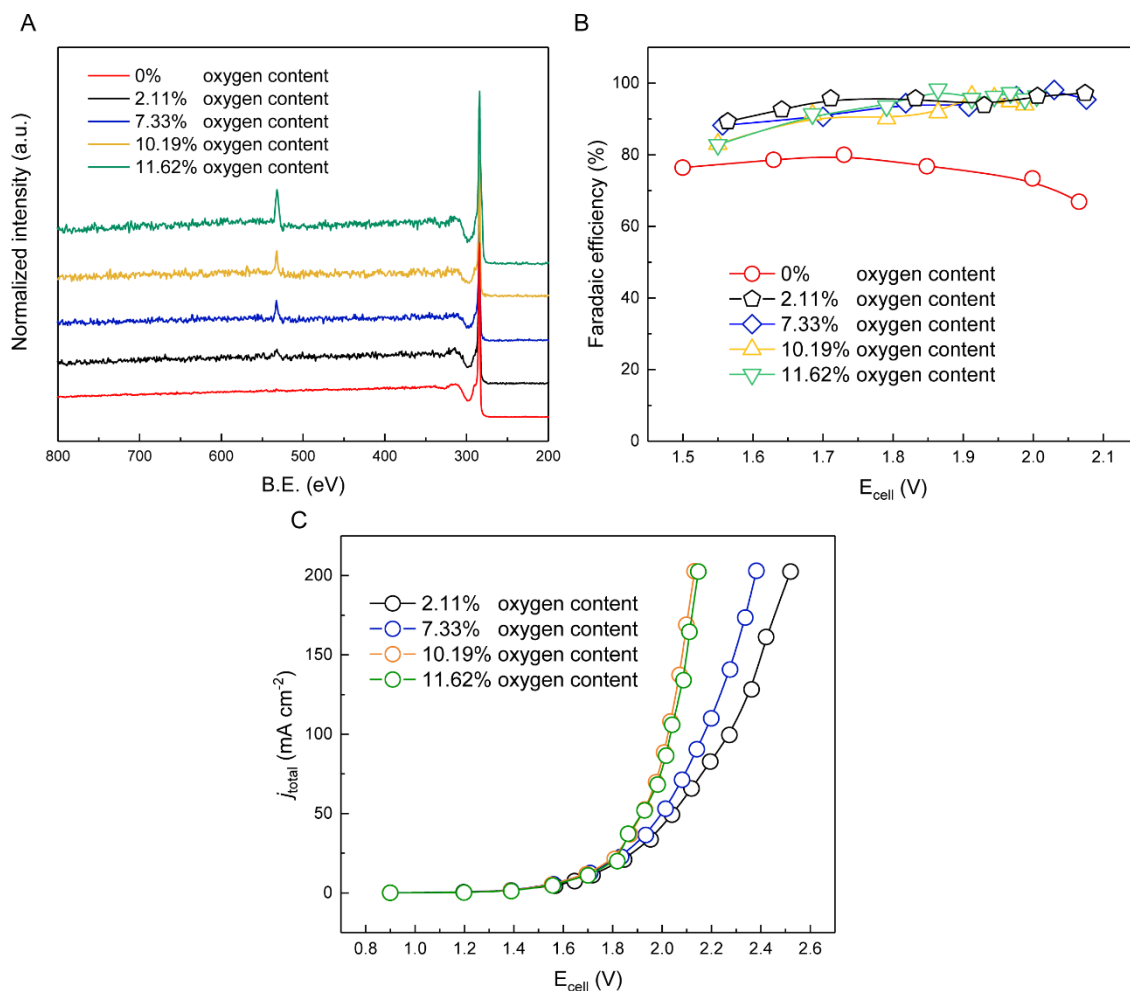


Fig. S5.

Tuning the surface oxygen on carbon black for optimized $2e^-$ -ORR performance. (A) XPS survey scans of carbon black catalysts with different surface oxygen contents. (B) Faradaic efficiencies and (C) I-V curves of carbon black catalysts with different surface oxygen contents for $2e^-$ -ORR using $\text{O}_2//\text{SE}/\text{H}_2\text{O}$ cell configuration with solid proton conductor (Fig. 3A). As shown in (B), carbon black catalyst without the surface oxygen functional groups (0 % oxygen) shows a H_2O_2 FE of $< 80\%$. With surface oxygen content increased to 2.11%, we found that the H_2O_2 FE of carbon black catalyst quickly ramped up to $\sim 95\%$. By further increasing the surface oxygen content (from 2.11 to 11.62%), we observed a gradual increase in ORR activity (current density) in fig. S5C due to the increased density of active sites. Please be noted here that the 3h and 12h oxidation of carbon black presents surface oxygen ratio of 10.19% and 11.62%, respectively. While we have extended the oxidation time by four times, only slight increase in oxygen content was observed, suggesting that the surface functional group oxygen is almost saturated using this method. They also showed quite similar ORR activity in (C). Therefore, considering the material preparation cost, we chose to use CB-3h catalyst (10.19% surface oxygen) in our study for the demonstration of pure H_2O_2 solution generation.

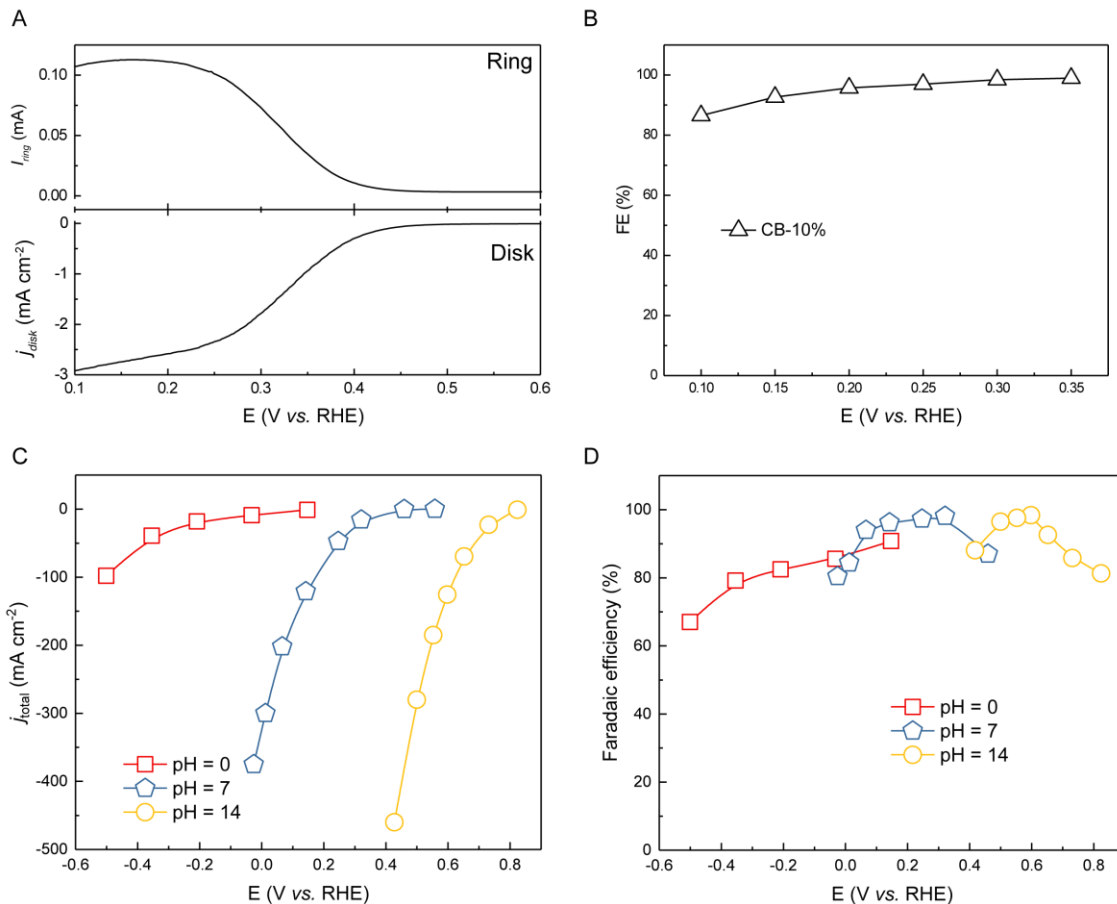


Fig. S6.

The intrinsic 2e⁻-ORR activity of CB-10%. (A) Linear sweep voltammetry (LSV) of CB-10% catalysts recorded at 1600 rpm and a scan rate of 5 mV s⁻¹, together with the detected H_2O_2 currents on the ring electrode (upper panel) at a fixed potential of 1.2 V vs. RHE. (B) The calculated H_2O_2 selectivity in 0.1 M Na_2SO_4 electrolyte using RRDE. (C) The I-V curve of ORR on CB-10% catalyst using the standard three-electrode setup in a traditional flow-cell system with 0.5 M H_2SO_4 (pH = 0), 1.0 M Na_2SO_4 (pH = 7) and 1.0 M KOH (pH = 14) as the liquid electrolyte. (D) The corresponding FEs of H_2O_2 under different potentials. As our focus is to produce pure H_2O_2 solutions, the most relevant evaluation of catalyst's performance is in neutral pH electrolyte. Since many recent reports of oxidized carbon materials have been evaluated in the alkaline or acidic electrolyte for 2e⁻-ORR, we therefore included the 2e⁻-ORR performance of our sample in alkaline and acidic solution for fair comparison.

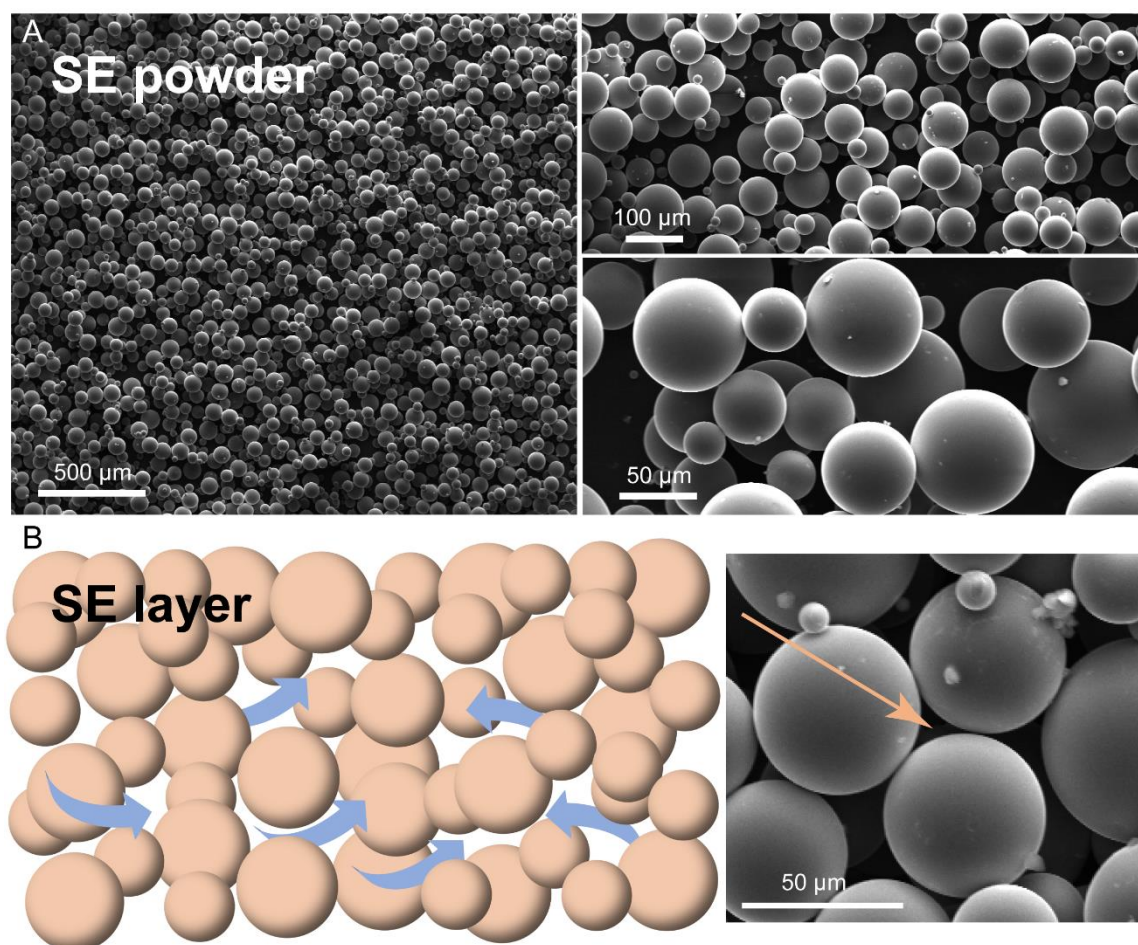


Fig. S7.

Characterization of solid electrolyte. (A) SEM image of solid polymer proton conductor. It shows that the average size of the as-obtained sulfonated styrene-divinylbenzene copolymer proton conductor is around 50 μm with uniform spherical morphology. (B) Schematic illustration and SEM image of solid electrolyte layer. Those solid electrolyte particles were densely packed into the thin middle layer to conduct protons during H_2O_2 generation. The micron pores between those polymer spheres form a tortuous pathway, allowing water flow and facilitating the releasing of produced H_2O_2 .

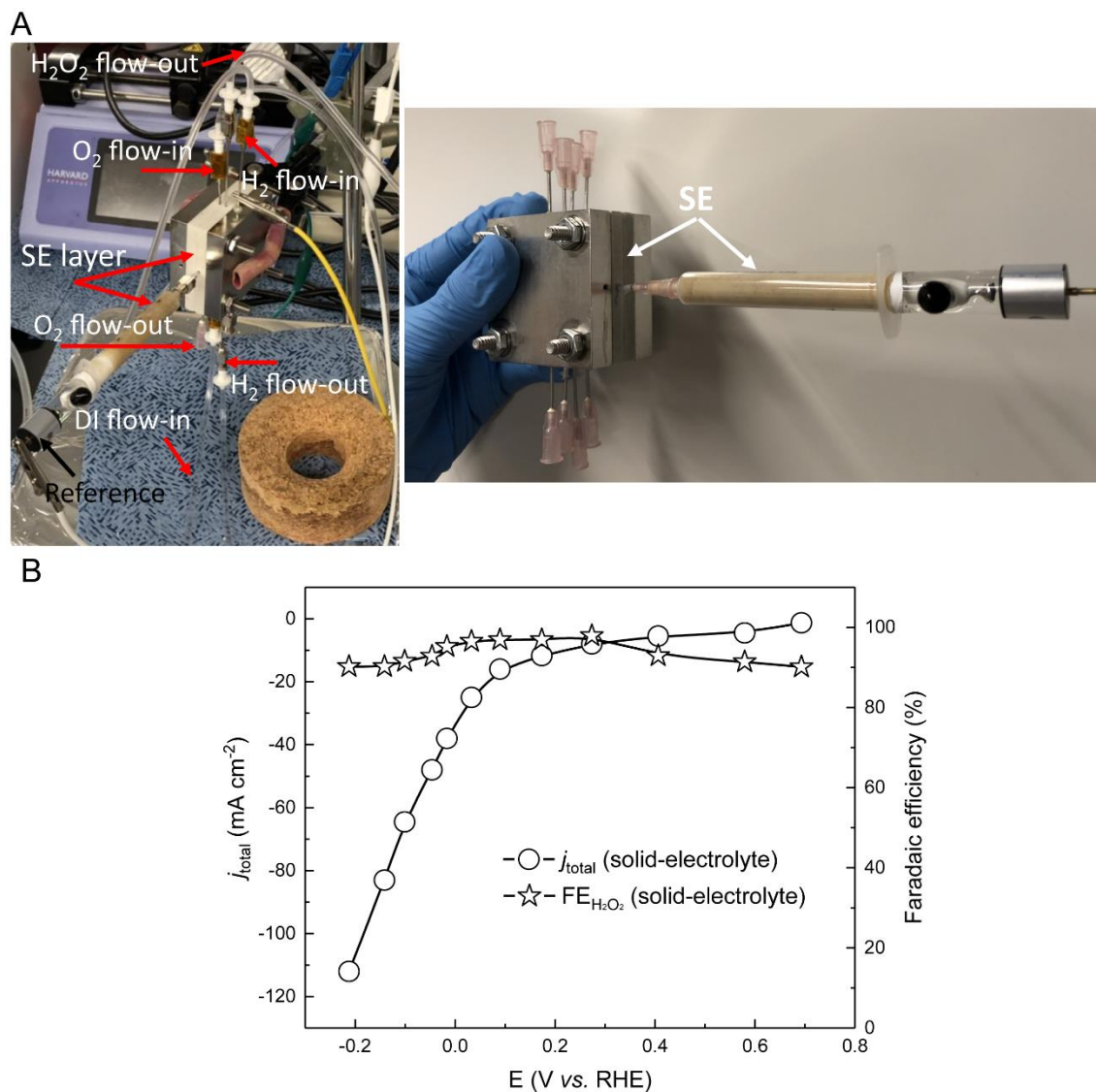


Fig. S8.

2e⁻-ORR performance of CB-10% in a standard three-electrode cell with solid electrolyte (Methods). (A) Digital photo of the three-electrode setup with solid electrolyte. (B) The 2e⁻-ORR performance of CB-10% catalyst. It shows that the excellent 2e⁻-ORR selectivity of CB-10% catalyst evaluated in traditional liquid electrolyte can be well maintained in solid electrolyte. The slightly increased overpotential may due to the increased charge transfer resistance in solid electrolyte cell compared to the liquid electrolyte one (61-63). The SE represents the polymer proton solid conductor.

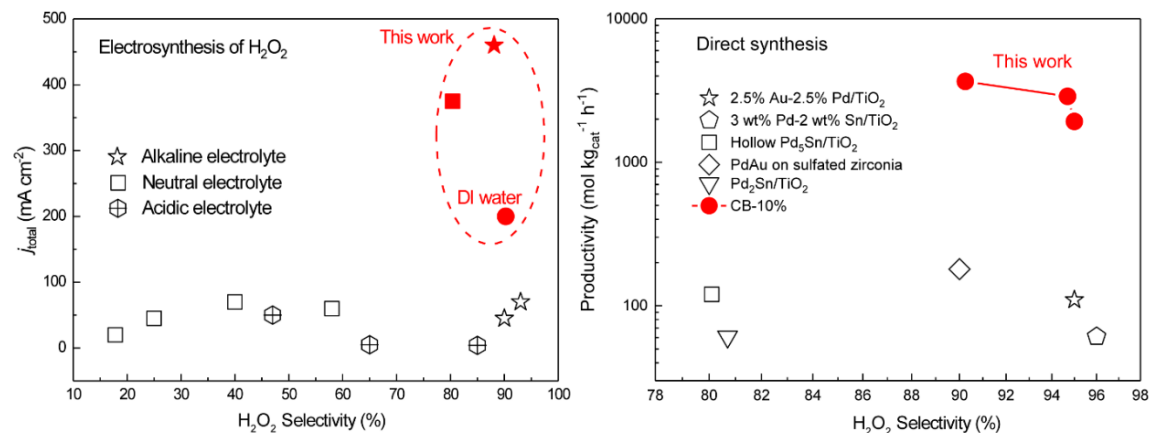


Fig. S9.

H_2O_2 productivity of our $\text{O}_2//\text{SE}//\text{H}_2$ system compared with previous literature. The data are reproduced from ref. 8, 9, and 45-47 (direct synthesis), and 19-21 and 48-53 (electrosynthesis). Our method demonstrated 1-2 orders of magnitude improved productivity compared to those direct synthesis cases. In addition, the H_2O_2 selectivity and current densities in both solid electrolytes (pure products) and different pH solutions are among the best compared to the state-of-the-art electrochemical synthesis strategies.

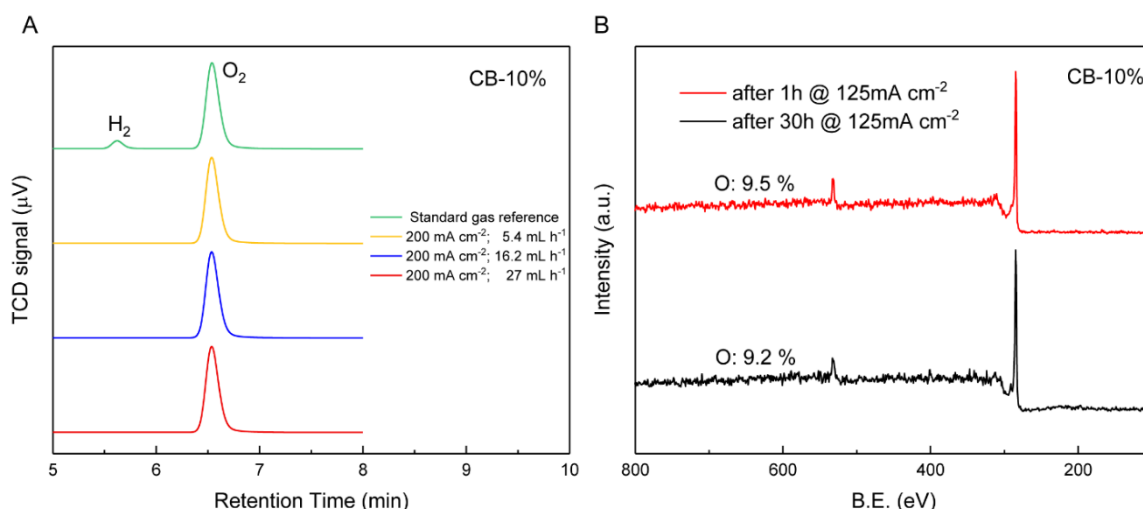


Fig. S10.

Online H₂ detection during H₂O₂ production and the XPS analysis of post-stability catalyst. (A) Gas chromatography analysis of cathode gas flow of CB-10%/SE//Pt-C cell during H₂O₂ production using O₂ and H₂. While the potential window of ORR reaction is more positive than HER, in our case, particularly under large current densities, large overpotentials might be needed, which could overlap with HER potential window. For example in fig. S8, we showed that -0.2 V *vs.* RHE is required for CB-10% catalyst to deliver a ORR current density of ~110 mA cm⁻² with solid electrolyte. We therefore used a gas chromatography to detect if there are any byproduct of H₂ particularly under high current densities (*e.g.* 200 mA cm⁻² cell current density). Our data shows that no H₂ signal can be detected (lower than the detection limit of the flame ionization detector). It demonstrates that the measured electrocatalytic cathodic current exclusively stemmed from oxygen reduction reaction, and there was no contribution from hydrogen evolution even when operated at such a high current density. (B) XPS survey scans of CB-10% catalyst after stability test under a relatively high current density. It shows that the surface oxygen content will decrease to 9.5% after 1 h stability test of CB-10% catalyst, then remain relatively stable to 9.2% after 30 h test. It suggests that some unstable surface oxygen was quickly reduced during ORR, but most of the surface functional groups were robust under ORR conditions, which guarantees the good stability for continuous generation of pure H₂O₂ solutions.

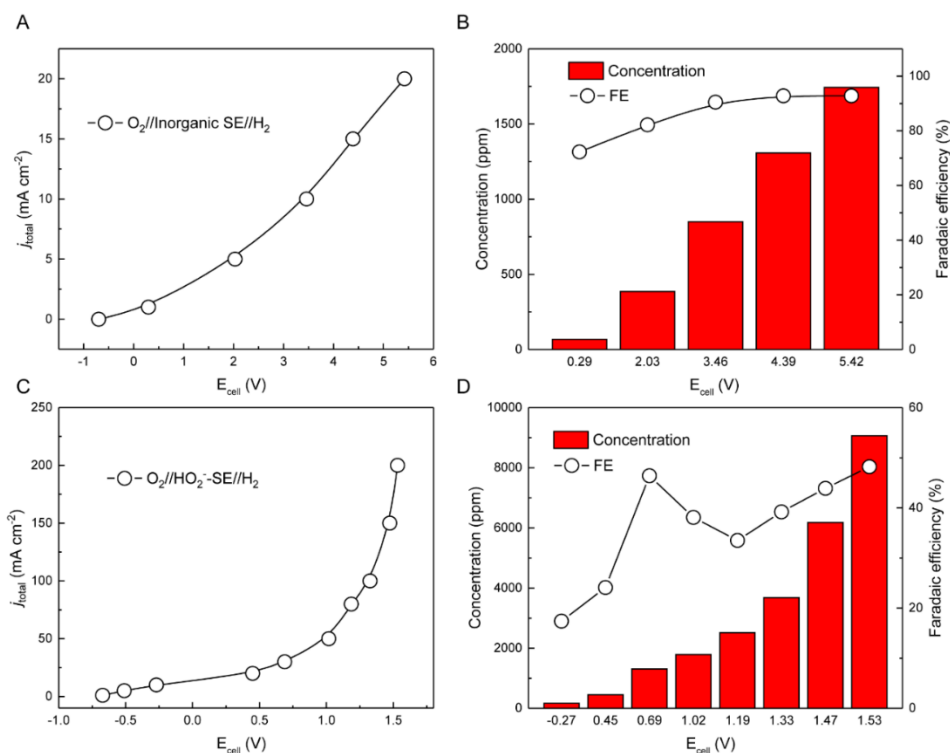


Fig. S11.

Pure H₂O₂ generation using O₂ and H₂ with polymer HO₂⁻ conductor and inorganic proton conductor. The current densities over cell voltages of CB-10%//SE//Pt-C cell with (A) inorganic Cs_xH_{3-x}PW₁₂O₄₀ proton solid conductor and (C) HO₂⁻ conducting solid-electrolyte. The corresponding FEs and concentration of H₂O₂ products under different cell voltages for (B) inorganic Cs_xH_{3-x}PW₁₂O₄₀ proton solid conductor and (D) HO₂⁻ conducting solid-electrolyte. Note that the DI flow-rate is 27 mL h⁻¹. The relatively low H₂O₂ FEs for cell using HO₂⁻ conducting solid-electrolyte is probably caused by the self-decomposition of H₂O₂ as significant gas bubbles was observed, as the HO₂⁻ conducting solid-electrolyte provides a high local alkaline environmental for ion-conduction. Based on the working mechanism of our device, the solid electrolyte we chose needs to satisfy the following two properties. First, the solid electrolyte should have high ion conductivity for efficient ion transportations and thus low ohmic-loss and high cell-efficiency; second, the solid electrolyte should be porous, thus water can flow through this layer to collect H₂O₂ product. In principle, different types of porous solid electrolyte, with different materials or different types of ion conductions (cation or anion), can be used in this system for pure H₂O₂ generation based on the same working mechanism. This may include ion conducting polymers with different functional groups, inorganic compounds, or other types of solid electrolyte materials such as ceramics, polymer/ceramic hybrids or solidified gels. Here, polymeric conductors for HO₂⁻ conduction and inorganic Cs_xH_{3-x}PW₁₂O₄₀ for cation conduction were also demonstrated to be effective for pure H₂O₂ solution generation, which suggests the wide tunability and versatility of our solid electrolyte design. Please note here that the different cell performances may be due to the different solid electrolyte properties.

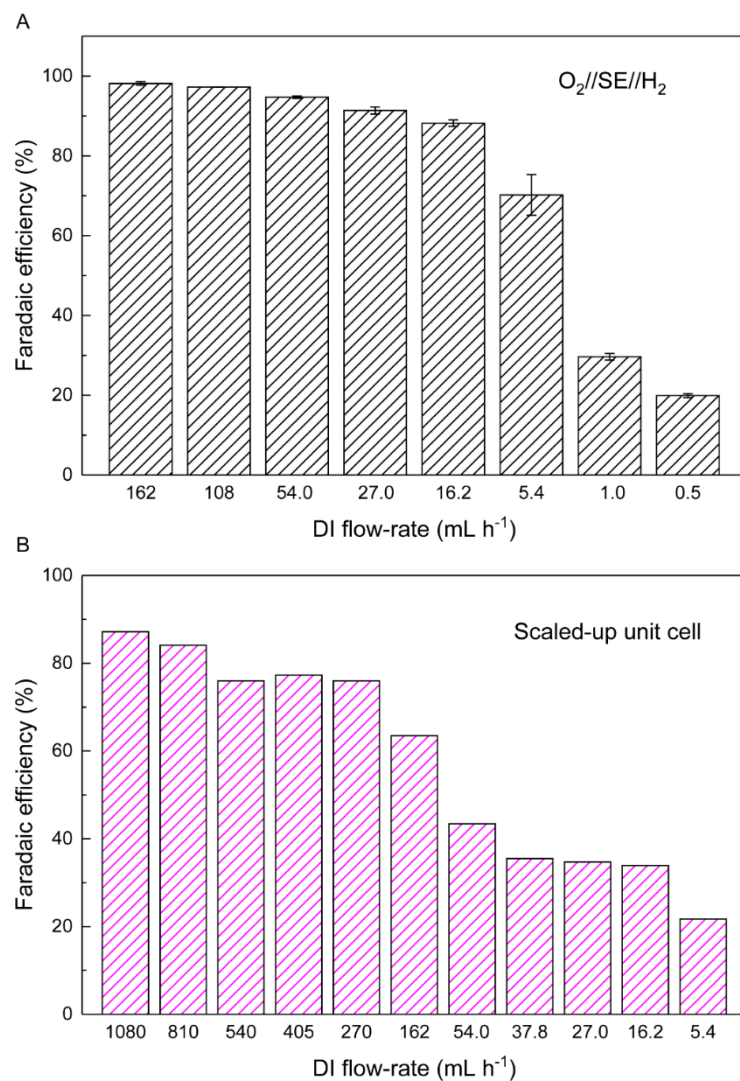


Fig. S12.

H₂O₂ generation performance of O₂//SE//H₂ and scaled up cell. H₂O₂ FEs as a function of DI water flow rate for (A) O₂//SE//H₂ under 200 mA cm⁻² (4 cm² cell) and (B) scaled-up O₂//SE//H₂O unit cell under 8 A (80 cm² cell), showing the H₂O₂ selectivity was decreased with increased H₂O₂ concentration.

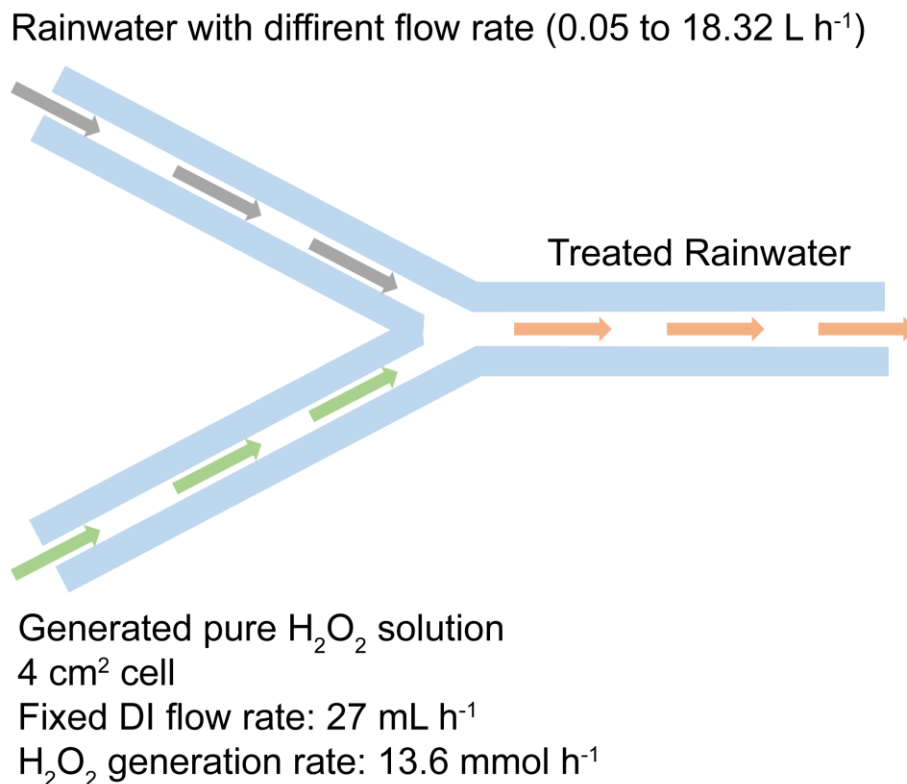


Fig. S13

Schematic illustration of the rainwater purification using on-site generated pure H_2O_2 solution. In our 4 cm^2 device experiments, we fixed our DI flow rate (27 mL h^{-1}) as well as H_2O_2 generation rate (13.6 mmol h^{-1}), therefore, the concentration of the H_2O_2 stream from our device is $\sim 0.5 \text{ M}$ ($17,000 \text{ ppm}$). The rainwater stream flow rate was tunable, ranging from the highest of 18.32 L h^{-1} to the lowest of 0.05 L h^{-1} . Therefore, once the DI flow with generated H_2O_2 was mixed with rainwater flow, the H_2O_2 concentration was diluted to a range from $\sim 25 \text{ ppm}$ to 6000 ppm . In general, with the rainwater flow rate (rainwater treatment rate) decreased, the H_2O_2 concentration in the mixture will be increased, which can decrease the remaining TOC. To meet the drinking water standards with the remaining TOC concentration lower than 2 ppm , the maximal rainwater treatment rate using our 4 cm^2 device is 0.88 L h^{-1} as shown in Fig. 2D. This represents a rainwater to DI flow rate ratio of 32.6 . Once normalized to the electrode area, this rainwater treatment rate by our design is $0.22 \text{ L cm}^{-2}_{\text{electrode}} \text{ h}^{-1}$ or $2200 \text{ L m}^{-2}_{\text{electrode}} \text{ h}^{-1}$.

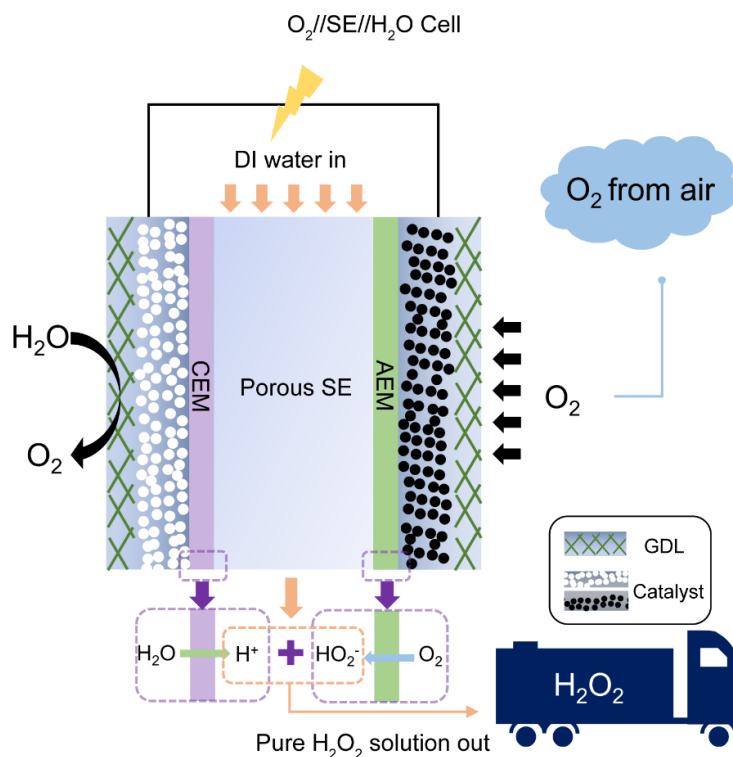


Fig. S14.

Electrosynthesis of H_2O_2 using pure H_2 and H_2O separately introduced to the anode and cathode, respectively. SE represents a solid electrolyte, which is sulfonated styrene-divinylbenzene copolymer microspheres. AEM and CEM represent anion and cation exchange membranes, respectively. Electrochemically generated cations (H^+) and anions (HO_2^-), driven by the electric field, cross in the porous SE layer and recombine to form H_2O_2 . DI water flowing through the porous SE layer then dissolves the H_2O_2 with no impurities.

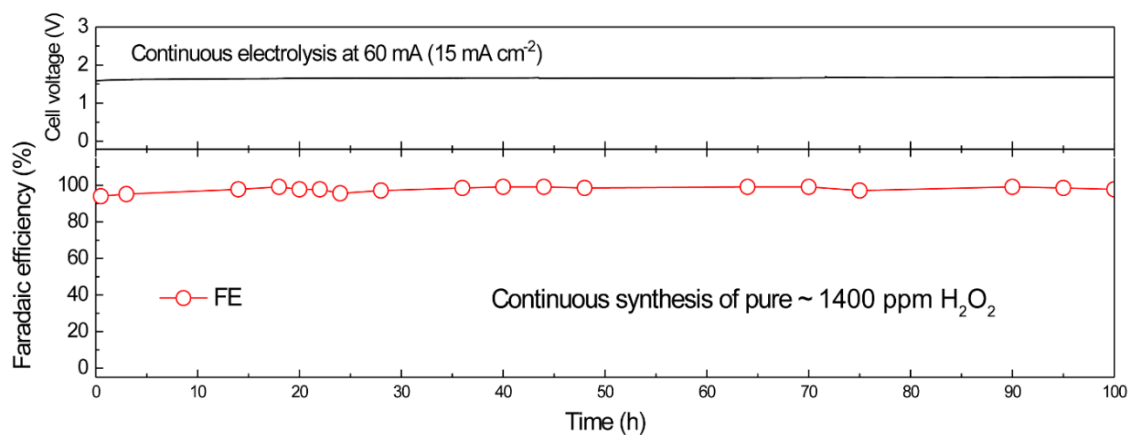


Fig. S15.

Stability of O₂//SE//H₂O cell. Long-term operation test of direct electrosynthesis of pure H₂O₂ solution using O₂//SE//H₂O cell, showing high selectivity stability at 60 mA using this proposed system. The FE of H₂O₂ maintains constant (~ 95%) over the 100-hour continuous operation. The DI flow-rate is 27 mL h⁻¹.

Supplementary Text:

Note 1: Comparison of previously reported polymer membrane design (ref. 19-21) with our strategy for pure H₂O₂ generation.

Yamanaka *et al.* (ref. 19) and Wilkinson *et al.* (ref. 20 and 21) reported the production of neutral H₂O₂ solution using a nafion membrane design similar to a H₂/O₂ fuel cell, as illustrated on the right. Although these cell designs have demonstrated neutral H₂O₂ generation, they suffered from low reaction rates, product concentrations, and Faradaic efficiencies. For the batch reactor (ref. 19), only 8 wt.% H₂O₂ solution can be produced after 6 h continuous electrolysis with FE of 26.5%. Moreover, in this case the maximal production rate for H₂O₂ is around 0.289 mmol cm⁻² h⁻¹. Wilkinson *et al.* (ref. 20 and 21) used a flow-through reactor to continuously produce the neutral H₂O₂. However, only small H₂O₂ production rate (0.2 mmol cm⁻² h⁻¹) can be achieved with a limited FE of ~ 30%. The maximal concentration of H₂O₂ is only 1400 ppm. As a comparison, in our strategy, we achieved high FE (> 90%) and production rate (3.4 mmol cm⁻² h⁻¹), as well as high product concentration (20 wt.%), outperforming those previous reports.

Based on our understanding, there might be several reasons for the lower performance in the previous nafion membrane design. First, the local H₂O₂ concentration might be high so that it retards its generation and lowers its selectivity. In this design, H₂O₂ molecules are formed and accumulated at the interface between ORR catalysts and membrane, which are then diffused into H₂O or brought out by O₂ gas flow. However, this product release rate is slower than that of our design where generated HO₂⁻ ions can quickly diffuse away into the middle layer as they are driven by the electrical field. Second, since the products are accumulated at the catalyst-membrane interface, the product collection efficiency might be low. Third, the local pH of the cation exchange membrane could also impact the catalysts' performance.

Here we also briefly analyze the extra membrane and solid electrolyte cost compared to the nafion membrane design. In our study, the cost of anion exchange membrane (AEM) is low. For example, the one from Membranes International Inc. is \$6480 for 1.2m × 36.50m size AEM, translating to only ~ \$148/m². Considering the impressive long-term stability, the net cost of the AEM is very low. Furthermore, we believe the cost for the solid electrolyte is also negligible based on the following considerations: 1) the main cost of the solid electrolyte is from the styrene-divinylbenzene copolymer which is only ~ \$2/kg, while the use in a 1 m² device could be only ~ 1.9 kg; 2) we found the solid electrolyte is very robust and no performance decay can be observed even after 3 times of long-term stability test. Considering the dramatically improved production rate and cell efficiency compared with previously reported designs, we believe that the extra cost for our design is negligible when the device is used for practical H₂O₂ generation.

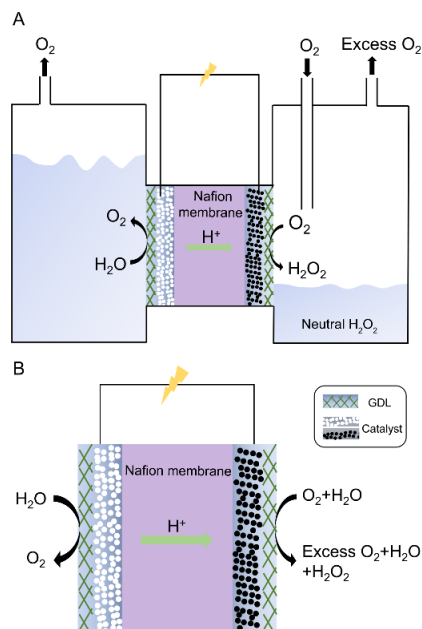


Fig. N1. Previously reported (A) batch and (B) flow thorough reactor for neutral H₂O₂ generation.

Note 2: N-doped carbon and adequately porous carbons for 2e⁻-ORR.

N-doped carbon and porous carbon have been previously reported for 2e⁻-ORR. Below we will discuss in detail about some advantages of the oxidized carbon black we used in this work compared to those reported catalysts.

First, the cost of catalyst synthesis is an important consideration in our study. While the above-mentioned metal-free catalysts showed very impressive 2e⁻-ORR performance, their synthesis costs could be higher compared to that of the oxidized carbon black. To be specific, in ref. 27, Iglesia *et al.* reported the beautiful synthesis of graphitized N-doped single-wall carbon nanohorns (g-N-CNHs) for H₂O₂ production. However, at least three steps are needed to prepare g-N-CNHs, which involve high temperature process (700 °C) and precursors like carbon nanohorns, dopamine hydrochloride and so on (higher cost than carbon black). In ref. 28, Fellingner *et al.* prepared mesoporous nitrogen-doped carbon derived from the ionic liquid N-butyl-3-methylpyridinium dicyanamide for 2e⁻-ORR, which is a more expensive precursor than carbon black. In ref. 29, Liu *et al.* prepared the highly porous carbon by annealing MOF-5 precursor at 1100 °C under H₂ or Ar atmosphere with a holding time of 5 h. In addition, the preparation of the MOF-5 precursor needs long aging time (36 h) and higher cost raw materials (*e.g.* 1,4-benzenedicarboxylic acid and N, N-dimethylformamide). Our high-performance CB-10% catalyst can be easily produced by refluxing commercial carbon black in nitric acid for 3 h under only 85 °C, which we believe is more economically viable than the above-mentioned cases.

Second but more importantly, while these mentioned catalysts showed impressive 2e⁻-ORR performances in acidic electrolyte, their 2e⁻-ORR performances are not as good as our catalyst in neutral pH. For example, g-N-CNHs catalyst (ref. 27) delivered an average H₂O₂ FE of ~70% in pH = 7.4 electrolyte; the porous carbon catalyst (ref. 29) showed a maximal H₂O₂ FE of ~80% in pH = 7 electrolyte.

Note 3: Exclusion of possible Pt contamination on ORR cathode in O₂//SE//H₂ cell.

It has been widely accepted in hydrogen evolution reaction tests that a Pt counter electrode should not be used for water oxidation. This is because trace amount of Pt ions could be dissolved in electrolyte due to the high OER working potentials, and then be electroplated onto the HER catalyst and contribute to its excellent performance. However, in this current work the situation is different. First, the Pt electrode in our cell is used for hydrogen oxidation, which has a much lower working potential than that of water oxidation. Under HOR reaction conditions Pt can be very stable as demonstrated in traditional H₂ fuel cells. We also confirmed by ICP-OER analysis that Pt ions were not detectable (lower than the detection limit of 50 ppb) in generated H₂O₂ solution from the middle layer (Supplementary Table S1). This result confirms that no Pt atoms migrate from the anode into the middle solid electrolyte layer, not to mention the cathode side. In addition, the anion exchange membrane separating the cathode and solid electrolyte layer functions as another layer of protection, since cations cannot be transported across the AEM into the cathode. Lastly, as further direct evidence, no Pt signal can be detected from the ORR catalyst electrode by XPS even after the 30-h stability test at 125 mA cm⁻² (fig. S10B)

Note 4: Preliminary estimation of the production cost for the electrosynthesis of H₂O₂ using the 4 cm² O₂//SE//H₂ and O₂//SE//H₂O cells. We only calculated the costs of energy and feedstock input; no other costs associated with practical production or infrastructure were included. As a reference, the commercial H₂O₂ price is ~ \$1.5/kg-H₂O₂ plus transportation cost (64, 65).

O₂//SE//H₂O cell:

Operation condition: 2.13 V (800 mA); Production rate: 3.3 mmol cm⁻² h⁻¹ (0.4488 g h⁻¹)

$$m_{H_2O_2} = \frac{1 \text{ kWh}}{2.13 \text{ V} * 0.8 \text{ A}} * 0.4488 \text{ g h}^{-1} = \sim 263.4 \text{ g}$$

Thus, we can obtain 0.2634 kg H₂O₂ using 1 kWh electricity. This 0.2634 kg H₂O₂ consumes 0.1239 kg O₂, where the industrial O₂ price is < \$0.1/kg (<https://www.intratec.us/chemical-markets/oxygen-price>), therefore the O₂ cost is 1.24 cents. We note here that O₂ gas produced from the anode side can be collected to reduce the O₂ cost. Assuming the price of electricity is 3 cents/kWh (66), we can roughly estimate a H₂O₂ production cost of *ca. \$0.16/kg-H₂O₂* without considering the cost of DI water. The industrial water in Texas is \$1.91 per 1000 gallon (<https://www.fbgtx.org/673/Industrial-Water-Rates>). Only 1 to 3 cents are needed to deionize one gallon of water (<https://blog.uswatersystems.com/2012/08/de-ionization-101/>). Thus, the price of DI water is estimated to be ~ 3 cents/gallon or \$0.008/kg, which only adds a marginal cost to the H₂O₂ production cost of \$0.16/kg.

O₂//SE//H₂ cell:

Operation condition: 0.61 V (800 mA); Production rate: 3.4 mmol cm⁻² h⁻¹ (0.4624 g h⁻¹)

$$m_{H_2O_2} = \frac{1 \text{ kWh}}{0.61 \text{ V} * 0.8 \text{ A}} * 0.4624 \text{ g h}^{-1} = \sim 947.5 \text{ g}$$

Thus, we can obtain 0.9475 kg H₂O₂ using 1 kWh electricity. This 0.9475 kg H₂O₂ consumes 0.0557 kg H₂ and 0.8918 kg O₂. The price of H₂ is ~ \$4/kg (67), and the price of O₂ is ~ \$0.1/kg. Assuming the price of renewable electricity is 3 cents/kWh (66), we can estimate a cost of *ca. \$0.34/kg-H₂O₂*.

The calculated cost of H₂O₂ from electrochemical synthesis will be even lower when a lower production rate is selected (higher energy conversion efficiency).

Supplementary Table S1. The concentration of impurities for generated H₂O₂ using O₂//SE//H₂O cell. Note that the reported concentrations are average results acquired from 5 independent tests.

Sodium	Iron	Sulfur	Platinum
0.872 ppm	0.022 ppm	2.62 ppm	Lower than detection limit

References and Notes

1. S. Yang, A. Verdaguer-Casadevall, L. Arnarson, L. Silvioli, V. Čolić, R. Frydendal, J. Rossmeisl, I. Chorkendorff, I. E. L. Stephens, Toward the decentralized electrochemical production of H₂O₂: A focus on the catalysis. *ACS Catal.* **8**, 4064–4081 (2018). [doi:10.1021/acscatal.8b00217](https://doi.org/10.1021/acscatal.8b00217)
2. Y. Yi, L. Wang, G. Li, H. Guo, A review on research progress in the direct synthesis of hydrogen peroxide from hydrogen and oxygen: Noble-metal catalytic method, fuel-cell method and plasma method. *Catal. Sci. Technol.* **6**, 1593–1610 (2016). [doi:10.1039/C5CY01567G](https://doi.org/10.1039/C5CY01567G)
3. R. J. Lewis, G. J. Hutchings, Recent advances in the direct synthesis of H₂O₂. *ChemCatChem* **11**, 298–308 (2019). [doi:10.1002/cctc.201801435](https://doi.org/10.1002/cctc.201801435)
4. J. K. Edwards, G. J. Hutchings, Palladium and gold-palladium catalysts for the direct synthesis of hydrogen peroxide. *Angew. Chem. Int. Ed.* **47**, 9192–9198 (2008). [doi:10.1002/anie.200802818](https://doi.org/10.1002/anie.200802818) [Medline](#)
5. J. H. Lunsford, The direct formation of H₂O₂ from H₂ and O₂ over palladium catalysts. *J. Catal.* **216**, 455–460 (2003). [doi:10.1016/S0021-9517\(02\)00070-2](https://doi.org/10.1016/S0021-9517(02)00070-2)
6. D. P. Dissanayake, J. H. Lunsford, Evidence for the role of colloidal palladium in the catalytic formation of H₂O₂ from H₂ and O₂. *J. Catal.* **206**, 173–176 (2002). [doi:10.1006/jcat.2001.3501](https://doi.org/10.1006/jcat.2001.3501)
7. J. K. Edwards, B. Solsona, E. N. N. A. F. Carley, A. A. Herzing, C. J. Kiely, G. J. Hutchings, Switching off hydrogen peroxide hydrogenation in the direct synthesis process. *Science* **323**, 1037–1041 (2009). [doi:10.1126/science.1168980](https://doi.org/10.1126/science.1168980) [Medline](#)
8. J. K. Edwards, E. Ntainjua, A. F. Carley, A. A. Herzing, C. J. Kiely, G. J. Hutchings, Direct synthesis of H₂O₂ from H₂ and O₂ over gold, palladium, and gold-palladium catalysts supported on acid-pretreated TiO₂. *Angew. Chem. Int. Ed.* **48**, 8512–8515 (2009). [doi:10.1002/anie.200904115](https://doi.org/10.1002/anie.200904115) [Medline](#)
9. S. J. Freakley, Q. He, J. H. Harrhy, L. Lu, D. A. Crole, D. J. Morgan, E. N. Ntainjua, J. K. Edwards, A. F. Carley, A. Y. Borisevich, C. J. Kiely, G. J. Hutchings, Palladium-tin catalysts for the direct synthesis of H₂O₂ with high selectivity. *Science* **351**, 965–968 (2016). [doi:10.1126/science.aad5705](https://doi.org/10.1126/science.aad5705) [Medline](#)
10. Q. Liu, J. C. Bauer, R. E. Schaak, J. H. Lunsford, Direct synthesis of H₂O₂ from H₂ and O₂ over Pd–Pt/SiO₂ bimetallic catalysts in a H₂SO₄/ethanol system. *Appl. Catal. A Gen.* **339**, 130–136 (2008). [doi:10.1016/j.apcata.2008.01.026](https://doi.org/10.1016/j.apcata.2008.01.026)
11. S. Abate, R. Arrigo, M. E. Schuster, S. Perathoner, G. Centi, A. Villa, D. Su, R. Schlögl, Pd nanoparticles supported on N-doped nanocarbon for the direct synthesis of H₂O₂ from H₂ and O₂. *Catal. Today* **157**, 280–285 (2010). [doi:10.1016/j.cattod.2010.01.027](https://doi.org/10.1016/j.cattod.2010.01.027)
12. Q. Liu, J. C. Bauer, R. E. Schaak, J. H. Lunsford, Supported palladium nanoparticles: An efficient catalyst for the direct formation of H₂O₂ from H₂ and O₂. *Angew. Chem. Int. Ed.* **47**, 6221–6224 (2008). [doi:10.1002/anie.200801517](https://doi.org/10.1002/anie.200801517) [Medline](#)
13. C. E. Baukal Jr., *Oxygen-Enhanced Combustion* (CRC, 2013).

14. S. Siahrostami, A. Verdaguer-Casadevall, M. Karamad, D. Deiana, P. Malacrida, B. Wickman, M. Escudero-Escribano, E. A. Paoli, R. Frydendal, T. W. Hansen, I. Chorkendorff, I. E. L. Stephens, J. Rossmeisl, Enabling direct H₂O₂ production through rational electrocatalyst design. *Nat. Mater.* **12**, 1137–1143 (2013). [doi:10.1038/nmat3795](https://doi.org/10.1038/nmat3795) [Medline](#)
15. H. W. Kim, M. B. Ross, N. Kornienko, L. Zhang, J. Guo, P. Yang, B. D. McCloskey, Efficient hydrogen peroxide generation using reduced graphene oxide-based oxygen reduction electrocatalysts. *Nat. Catal.* **1**, 282–290 (2018). [doi:10.1038/s41929-018-0044-2](https://doi.org/10.1038/s41929-018-0044-2)
16. Z. Lu, G. Chen, S. Siahrostami, Z. Chen, K. Liu, J. Xie, L. Liao, T. Wu, D. Lin, Y. Liu, T. F. Jaramillo, J. K. Nørskov, Y. Cui, High-efficiency oxygen reduction to hydrogen peroxide catalysed by oxidized carbon materials. *Nat. Catal.* **1**, 156–162 (2018). [doi:10.1038/s41929-017-0017-x](https://doi.org/10.1038/s41929-017-0017-x)
17. S. Chen, Z. Chen, S. Siahrostami, D. Higgins, D. Nordlund, D. Sokaras, T. R. Kim, Y. Liu, X. Yan, E. Nilsson, R. Sinclair, J. K. Nørskov, T. F. Jaramillo, Z. Bao, Designing boron nitride islands in carbon materials for efficient electrochemical synthesis of hydrogen peroxide. *J. Am. Chem. Soc.* **140**, 7851–7859 (2018). [doi:10.1021/jacs.8b02798](https://doi.org/10.1021/jacs.8b02798) [Medline](#)
18. S. Chen, Z. Chen, S. Siahrostami, T. R. Kim, D. Nordlund, D. Sokaras, S. Nowak, J. W. F. To, D. Higgins, R. Sinclair, J. K. Nørskov, T. F. Jaramillo, Z. Bao, Defective carbon-based materials for the electrochemical synthesis of hydrogen peroxide. *ACS Sustain. Chem. Eng.* **6**, 311–317 (2017). [doi:10.1021/acssuschemeng.7b02517](https://doi.org/10.1021/acssuschemeng.7b02517)
19. I. Yamanaka, T. Murayama, Neutral H₂O₂ synthesis by electrolysis of water and O₂. *Angew. Chem. Int. Ed.* **47**, 1900–1902 (2008). [doi:10.1002/anie.200704431](https://doi.org/10.1002/anie.200704431) [Medline](#)
20. W. Li, A. Bonakdarpour, E. Gyenge, D. P. Wilkinson, Drinking water purification by electrosynthesis of hydrogen peroxide in a power-producing PEM fuel cell. *ChemSusChem* **6**, 2137–2143 (2013). [doi:10.1002/cssc.201300225](https://doi.org/10.1002/cssc.201300225) [Medline](#)
21. W. T. Li, A. Bonakdarpour, E. Gyenge, D. P. Wilkinson, Design of bifunctional electrodes for co-generation of electrical power and hydrogen peroxide. *J. Appl. Electrochem.* **48**, 985–993 (2018). [doi:10.1007/s10800-018-1232-0](https://doi.org/10.1007/s10800-018-1232-0)
22. D. W. Flaherty, Direct synthesis of H₂O₂ from H₂ and O₂ on Pd catalysts: Current understanding, outstanding questions, and research needs. *ACS Catal.* **8**, 1520–1527 (2018). [doi:10.1021/acscatal.7b04107](https://doi.org/10.1021/acscatal.7b04107)
23. X. Tian, P. Zhao, W. Sheng, Hydrogen evolution and oxidation: Mechanistic studies and material advances. *Adv. Mater.* **31**, e1808066 (2019). [doi:10.1002/adma.201808066](https://doi.org/10.1002/adma.201808066) [Medline](#)
24. W. Sheng, H. A. Gasteiger, Y. Shao-Horn, Hydrogen oxidation and evolution reaction kinetics on platinum: Acid vs alkaline electrolytes. *J. Electrochem. Soc.* **157**, B1529–B1536 (2010). [doi:10.1149/1.3483106](https://doi.org/10.1149/1.3483106)
25. M. S. Wilson, S. Gottesfeld, High performance catalyzed membranes of ultra-low Pt loadings for polymer electrolyte fuel cells. *J. Electrochem. Soc.* **139**, L28–L30 (1992). [doi:10.1149/1.2069277](https://doi.org/10.1149/1.2069277)

26. J. S. Jirkovský, I. Panas, E. Ahlberg, M. Halasa, S. Romani, D. J. Schiffrin, Single atom hot-spots at Au-Pd nanoalloys for electrocatalytic H₂O₂ production. *J. Am. Chem. Soc.* **133**, 19432–19441 (2011). [doi:10.1021/ja206477z](https://doi.org/10.1021/ja206477z) [Medline](#)
27. L. Han, Y. Sun, S. Li, C. Cheng, C. E. Halbig, P. Feicht, J. L. Hübner, P. Strasser, S. Eigler, In-plane carbon lattice-defect regulating electrochemical oxygen reduction to hydrogen peroxide production over nitrogen-doped graphene. *ACS Catal.* **9**, 1283–1288 (2019). [doi:10.1021/acscatal.8b03734](https://doi.org/10.1021/acscatal.8b03734)
28. D. Iglesias, A. Giuliani, M. Melchionna, S. Marchesan, A. Criado, L. Nasi, M. Bevilacqua, C. Tavagnacco, F. Vizza, M. Prato, P. Fornasiero, N-doped graphitized carbon nanohorns as a forefront electrocatalyst in highly selective O₂ reduction to H₂O₂. *Chem* **4**, 106–123 (2018). [doi:10.1016/j.chempr.2017.10.013](https://doi.org/10.1016/j.chempr.2017.10.013)
29. T.-P. Feller, F. Hasché, P. Strasser, M. Antonietti, Mesoporous nitrogen-doped carbon for the electrocatalytic synthesis of hydrogen peroxide. *J. Am. Chem. Soc.* **134**, 4072–4075 (2012). [doi:10.1021/ja300038p](https://doi.org/10.1021/ja300038p) [Medline](#)
30. Y. Liu, X. Quan, X. Fan, H. Wang, S. Chen, High-yield electrosynthesis of hydrogen peroxide from oxygen reduction by hierarchically porous carbon. *Angew. Chem. Int. Ed.* **54**, 6837–6841 (2015). [doi:10.1002/anie.201502396](https://doi.org/10.1002/anie.201502396) [Medline](#)
31. S. C. Perry, D. Pangotra, L. Vieira, L.-I. Csepei, V. Sieber, L. Wang, C. Ponce de León, F. C. Walsh, Electrochemical synthesis of hydrogen peroxide from water and oxygen. *Nat. Rev. Chem.* **3**, 442–458 (2019). [doi:10.1038/s41570-019-0110-6](https://doi.org/10.1038/s41570-019-0110-6)
32. S. Günday, A. Bozkurt, W. H. Meyer, G. Wegner, Effects of different acid functional groups on proton conductivity of polymer-1, 2, 4-triazole blends. *J. Polym. Sci. B* **44**, 3315–3322 (2006). [doi:10.1002/polb.20956](https://doi.org/10.1002/polb.20956)
33. W. A. England, M. Cross, A. Hamnett, P. Wiseman, J. B. Goodenough, Fast proton conduction in inorganic ion-exchange compounds. *Solid State Ion.* **1**, 231–249 (1980). [doi:10.1016/0167-2738\(80\)90007-7](https://doi.org/10.1016/0167-2738(80)90007-7)
34. L. Fan, S. Wei, S. Li, Q. Li, Y. Lu, Recent progress of the solid-state electrolytes for high-energy metal-based batteries. *Adv. Energy Mater.* **8**, 1702657 (2018). [doi:10.1002/aenm.201702657](https://doi.org/10.1002/aenm.201702657)
35. Q. Zhao, X. Liu, S. Stalin, K. Khan, L. A. Archer, Solid-state polymer electrolytes with in-built fast interfacial transport for secondary lithium batteries. *Nat. Energy* **4**, 365–373 (2019). [doi:10.1038/s41560-019-0349-7](https://doi.org/10.1038/s41560-019-0349-7)
36. S. H. Lee, J. C. Rasaiah, Proton transfer and the mobilities of the H⁺ and OH⁻ ions from studies of a dissociating model for water. *J. Chem. Phys.* **135**, 124505 (2011). [doi:10.1063/1.3632990](https://doi.org/10.1063/1.3632990) [Medline](#)
37. F. M. Coutinho, S. M. Rezende, B. G. Soares, Characterization of sulfonated poly (styrene-divinylbenzene) and poly (divinylbenzene) and its application as catalysts in esterification reaction. *J. Appl. Polym. Sci.* **102**, 3616–3627 (2006). [doi:10.1002/app.24046](https://doi.org/10.1002/app.24046)
38. R. C. Weast, M. J. Astle, W. H. Beyer, *CRC Handbook of Chemistry and Physics* (CRC, 1988), vol. 69.

39. K. J. Jeong, C. M. Miesse, J.-H. Choi, J. Lee, J. Han, S. P. Yoon, S. W. Nam, T.-H. Lim, T. G. Lee, Fuel crossover in direct formic acid fuel cells. *J. Power Sources* **168**, 119–125 (2007). [doi:10.1016/j.jpowsour.2007.02.062](https://doi.org/10.1016/j.jpowsour.2007.02.062)
40. Z. M. Galbács, L. J. Csányi, Alkali-induced decomposition of hydrogen peroxide. *J. Chem. Soc., Dalton Trans.* **11**, 2353–2357 (1983). [doi:10.1039/DT9830002353](https://doi.org/10.1039/DT9830002353)
41. M. Ravikumar, A. Shukla, Effect of methanol crossover in a liquid-feed polymer-electrolyte direct methanol fuel cell. *J. Electrochem. Soc.* **143**, 2601–2606 (1996). [doi:10.1149/1.1837054](https://doi.org/10.1149/1.1837054)
42. B. D. Black, G. W. Harrington, P. C. Singer, Reducing cancer risks by improving organic carbon removal. *J. Am. Water Works Assoc.* **88**, 40–52 (1996). [doi:10.1002/j.1551-8833.1996.tb06570.x](https://doi.org/10.1002/j.1551-8833.1996.tb06570.x)
43. A. Wenzel, A. Gahr, R. Niessner, TOC-removal and degradation of pollutants in leachate using a thin-film photoreactor. *Water Res.* **33**, 937–946 (1999). [doi:10.1016/S0043-1354\(98\)00302-9](https://doi.org/10.1016/S0043-1354(98)00302-9)
44. Texas Commission on Environmental Quality, *Total Organic Carbon (TOC) Guidance Manual*; https://tceq.texas.gov/assets/public/comm_exec/pubs/rg/rg-379.pdf.
45. P. Biasi, F. Menegazzo, F. Pinna, K. Eränen, T. O. Salmi, P. Canu, Continuous H₂O₂ direct synthesis over PdAu catalysts. *Chem. Eng. J.* **176–177**, 172–177 (2011). [doi:10.1016/j.cej.2011.05.073](https://doi.org/10.1016/j.cej.2011.05.073)
46. J. Zhang, Q. Shao, Y. Zhang, S. Bai, Y. Feng, X. Huang, Promoting the direct H₂O₂ generation catalysis by using hollow Pd–Sn intermetallic nanoparticles. *Small* **14**, 1703990 (2018). [doi:10.1002/sml.201703990](https://doi.org/10.1002/sml.201703990)
47. F. Li, Q. Shao, M. Hu, Y. Chen, X. Huang, Hollow Pd–Sn nanocrystals for efficient direct H₂O₂ synthesis: The critical role of Sn on structure evolution and catalytic performance. *ACS Catal.* **8**, 3418–3423 (2018). [doi:10.1021/acscatal.8b00347](https://doi.org/10.1021/acscatal.8b00347)
48. I. Yamanaka, T. Hashimoto, R. Ichihashi, K. Otsuka, Direct synthesis of H₂O₂ acid solutions on carbon cathode prepared from activated carbon and vapor-growing-carbon-fiber by a H₂/O₂ fuel cell. *Electrochim. Acta* **53**, 4824–4832 (2008). [doi:10.1016/j.electacta.2008.02.009](https://doi.org/10.1016/j.electacta.2008.02.009)
49. I. Yamanaka, T. Onizawa, S. Takenaka, K. Otsuka, Direct and continuous production of hydrogen peroxide with 93% selectivity using a fuel-cell system. *Angew. Chem. Int. Ed.* **42**, 3653–3655 (2003). [doi:10.1002/anie.200351343](https://doi.org/10.1002/anie.200351343) [Medline](#)
50. I. Yamanaka, T. Onizawa, H. Suzuki, N. Hanaizumi, K. Otsuka, Electrocatalysis of heat-treated Mn–porphyrin/carbon cathode for synthesis of H₂O₂ acid solutions by H₂/O₂ fuel cell method. *Chem. Lett.* **35**, 1330–1331 (2006). [doi:10.1246/cl.2006.1330](https://doi.org/10.1246/cl.2006.1330)
51. H. J. Luo, C. L. Li, C. Q. Wu, X. Q. Dong, In situ electrosynthesis of hydrogen peroxide with an improved gas diffusion cathode by rolling carbon black and PTFE. *RSC Advances* **5**, 65227–65235 (2015). [doi:10.1039/C5RA09636G](https://doi.org/10.1039/C5RA09636G)
52. A. Da Pozzo, L. Di Palma, C. Merli, E. Petrucci, An experimental comparison of a graphite electrode and a gas diffusion electrode for the cathodic production of hydrogen peroxide. *J. Appl. Electrochem.* **35**, 413–419 (2005). [doi:10.1007/s10800-005-0800-2](https://doi.org/10.1007/s10800-005-0800-2)

53. Z. Chen, S. Chen, S. Siahrostami, P. Chakthranont, C. Hahn, D. Nordlund, S. Dimosthenis, J. K. Nørskov, Z. Bao, T. F. Jaramillo, Development of a reactor with carbon catalysts for modular-scale, low-cost electrochemical generation of H₂O₂. *React. Chem. Eng.* **2**, 239–245 (2017). [doi:10.1039/C6RE00195E](https://doi.org/10.1039/C6RE00195E)
54. K. Jiang, S. Siahrostami, A. J. Akey, Y. Li, Z. Lu, J. Lattimer, Y. Hu, C. Stokes, M. Gangishetty, G. Chen, Y. Zhou, W. Hill, W.-B. Cai, D. Bell, K. Chan, J. K. Nørskov, Y. Cui, H. Wang, Transition-metal single atoms in a graphene shell as active centers for highly efficient artificial photosynthesis. *Chem* **3**, 950–960 (2017). [doi:10.1016/j.chempr.2017.09.014](https://doi.org/10.1016/j.chempr.2017.09.014)
55. J. Millar, D. Smith, W. Marr, T. Kressman, Solvent-modified polymer networks. Part I. The preparation and characterisation of expanded-network and macroporous styrene–divinylbenzene copolymers and their sulphonates. *J. Chem. Soc.* **0**, 218–225 (1963). [doi:10.1039/JR9630000218](https://doi.org/10.1039/JR9630000218)
56. T. Okuhara, H. Watanabe, T. Nishimura, K. Inumaru, M. Misono, Microstructure of cesium hydrogen salts of 12-tungstophosphoric acid relevant to novel acid catalysis. *Chem. Mater.* **12**, 2230–2238 (2000). [doi:10.1021/cm9907561](https://doi.org/10.1021/cm9907561)
57. K. A. Wepasnick, B. A. Smith, J. L. Bitter, D. Howard Fairbrother, Chemical and structural characterization of carbon nanotube surfaces. *Anal. Bioanal. Chem.* **396**, 1003–1014 (2010). [doi:10.1007/s00216-009-3332-5](https://doi.org/10.1007/s00216-009-3332-5) [Medline](#)
58. W. Zhou, L. Rajic, L. Chen, K. Kou, Y. Ding, X. Meng, Y. Wang, B. Mulaw, J. Gao, Y. Qin, A. N. Alshawabkeh, Activated carbon as effective cathode material in iron-free Electro-Fenton process: Integrated H₂O₂ electrogeneration, activation, and pollutants adsorption. *Electrochim. Acta* **296**, 317–326 (2019). [doi:10.1016/j.electacta.2018.11.052](https://doi.org/10.1016/j.electacta.2018.11.052) [Medline](#)
59. A. J. Plomp, D. S. Su, K. Jong, J. H. Bitter, On the nature of oxygen-containing surface groups on carbon nanofibers and their role for platinum deposition: An XPS and titration study. *J. Phys. Chem. C* **113**, 9865–9869 (2009). [doi:10.1021/jp900637q](https://doi.org/10.1021/jp900637q)
60. P. Wang, S. Zhan, Y. Xia, S. Ma, Q. Zhou, Y. Li, The fundamental role and mechanism of reduced graphene oxide in rGO/Pt-TiO₂ nanocomposite for high-performance photocatalytic water splitting. *Appl. Catal. B* **207**, 335–346 (2017). [doi:10.1016/j.apcatb.2017.02.031](https://doi.org/10.1016/j.apcatb.2017.02.031)
61. J. B. Vennekoetter, R. Sengpiel, M. Wessling, Beyond the catalyst: How electrode and reactor design determine the product spectrum during electrochemical CO₂ reduction. *Chem. Eng. J.* **364**, 89–101 (2019). [doi:10.1016/j.cej.2019.01.045](https://doi.org/10.1016/j.cej.2019.01.045)
62. F. Sagane, T. Abe, Y. Iriyama, Z. Ogumi, Li⁺ and Na⁺ transfer through interfaces between inorganic solid electrolytes and polymer or liquid electrolytes. *J. Power Sources* **146**, 749–752 (2005). [doi:10.1016/j.jpowsour.2005.03.075](https://doi.org/10.1016/j.jpowsour.2005.03.075)
63. Y. Iriyama, T. Kako, C. Yada, T. Abe, Z. Ogumi, Charge transfer reaction at the lithium phosphorus oxynitride glass electrolyte/lithium cobalt oxide thin film interface. *Solid State Ion.* **176**, 2371–2376 (2005). [doi:10.1016/j.ssi.2005.02.025](https://doi.org/10.1016/j.ssi.2005.02.025)
64. USP Technologies, How much does H₂O₂ cost?; <http://www.h2o2.com/faqs/FaqDetail.aspx?fld=25>.

65. K. Fuku, Y. Miyase, Y. Miseki, T. Gunji, K. Sayama, Enhanced oxidative hydrogen peroxide production on conducting glass anodes modified with metal oxides. *ChemistrySelect* **1**, 5721–5726 (2016). [doi:10.1002/slct.201601469](https://doi.org/10.1002/slct.201601469)
66. S. Chu, Y. Cui, N. Liu, The path towards sustainable energy. *Nat. Mater.* **16**, 16–22 (2016). [doi:10.1038/nmat4834](https://doi.org/10.1038/nmat4834) [Medline](#)
67. Argonne National Laboratory, *Hydrogen Demand, Production, and Cost by Region to 2050*; <https://publications.anl.gov/anlpubs/2005/09/54462.pdf>.